

Catalysis Science & Technology

Accepted Manuscript



This is an *Accepted Manuscript*, which has been through the Royal Society of Chemistry peer review process and has been accepted for publication.

Accepted Manuscripts are published online shortly after acceptance, before technical editing, formatting and proof reading. Using this free service, authors can make their results available to the community, in citable form, before we publish the edited article. We will replace this *Accepted Manuscript* with the edited and formatted *Advance Article* as soon as it is available.

You can find more information about *Accepted Manuscripts* in the [Information for Authors](#).

Please note that technical editing may introduce minor changes to the text and/or graphics, which may alter content. The journal's standard [Terms & Conditions](#) and the [Ethical guidelines](#) still apply. In no event shall the Royal Society of Chemistry be held responsible for any errors or omissions in this *Accepted Manuscript* or any consequences arising from the use of any information it contains.

CO Oxidation Activity of Thermally Stable Fe–Cu/CeO₂ Catalysts

Prepared by Dual-mode Arc-plasma Process

Satoshi Hinokuma^{1,2,3}, Noriko Yamashita¹,
Yasuo Katsuhara¹, Hayato Kogami¹, Masato Machida^{1,2*}

¹*Department of Applied Chemistry and Biochemistry,
Graduate School of Science and Technology, Kumamoto University,
2-39-1 Kurokami, Chuo, Kumamoto, 860-8555 Japan*

²*Unit of Elements Strategy Initiative for Catalysts & Batteries, Kyoto University
Kyoto Daigaku Katsura, Saikyo, Kyoto, 615-8520 Japan*

³*Japan Science and Technology Agency, Precursory Research for Embryonic Science and
Technology, 4-1-8 Honcho, Kawaguchi, Saitama, 332-0012, Japan*

CORRESPONDING AUTHOR:

Prof. Masato Machida

Department of Applied Chemistry and Biochemistry,

Graduate School of Science and Technology,

Kumamoto University,

2-39-1 Kurokami, Chuo, Kumamoto, 860-8555 Japan

TEL/FAX:+81-96-342-3651

E-mail: machida@kumamoto-u.ac.jp

Abstract

Fe–Cu bimetal nanoparticles were deposited on CeO₂ powders at a low loading level (≤ 0.2 wt%) by the dual-mode arc-plasma (AP) process. The bimetal particles enabled the formation of Fe–Cu oxide after being thermally aged at 900 °C, which was characterised by a highly dispersed Cu⁺ and Fe³⁺ on the surface of CeO₂. The CO oxidation activity was enhanced by thermal aging at 900 °C when prepared by the AP process compared to conventional wet-impregnation method, despite the significant decrease in surface area from 170 m²·g⁻¹ to less than 10 m²·g⁻¹. The higher activity can be rationalised by the more efficient formation of Fe–Cu oxide, the Cu⁺ species of which plays a role of CO chemisorption site. The reaction rate of CO oxidation exhibited partial orders of ~ 0.9 and ~ 0.0 with respect to CO and O₂, respectively. Pulsed C¹⁶O–¹⁸O₂ reactions revealed that CO adsorbed on Cu⁺ reacted mainly with lattice oxygen, which implies that the reaction proceeds *via* the Mars–van Krevelen mechanism.

Keywords: Arc-plasma process, Fe, Cu, CeO₂, CO oxidation, Mars–van Krevelen mechanism

1. Introduction

The most common conventional preparation method for supported metal and/or metal oxide catalysts consists of wet-impregnation of precursor solutions, drying and calcination under oxidising and/or reducing conditions. On the other hand, dry catalyst preparation using plasmas has attracted considerable attention because of its potential merits, which include (1) a highly dispersed active species, (2) reduced energy requirements, (3) enhanced catalyst activity and lifetime and (4) shortened preparation time.¹⁻⁴ We have recently reported a novel method for the preparation of supported catalysts using pulsed arc-plasma (AP).⁵⁻⁹ Unlike conventional multi-step wet-impregnation processes, AP enables the one-step deposition of highly dispersed metal nanoparticles from bulk metals onto the surface of support powders. The as-prepared catalysts showed higher catalytic activities because of their highly dispersed metal nanoparticles. Another advantage is the potential applications to bimetal nanoparticles by using dual-mode AP. One typical example is the Fe–Pd bimetal nanoparticles in our previous report.¹⁰ By synchronizing two pulsed arc-plasmas, bimetal nanoparticles consisting of homogeneously mixed Fe and Pd could be deposited on CeO₂ powders. The most important feature of as-prepared Fe–Pd/CeO₂ is the higher catalytic activities for CO oxidation than Pd/CeO₂, indicating the possibility to lessen the amount of precious metals with keeping the high catalytic performance in a wide range of applications. In this regard, it should be more promising to apply the dual-mode AP process to various non-precious metal systems as substitutes for precious metal catalysts.

Cu loaded on CeO₂ has been demonstrated to be a promising candidate alternative catalyst because of its efficient activity for CO oxidation under an oxygen-excess condition.¹¹⁻¹⁸ The high dispersion of Cu as a result of interactions with CeO₂ is believed to play key roles in the catalytic performance. Moreover, Fe–Cu/CeO₂ catalysts prepared by a

wet process were reported to exhibit higher catalytic performance for CO and CH₄ oxidation than CeO₂-supported Fe or Cu catalysts.^{19–24} Lenzion-Bielun et al. reported that the addition of approximately 2 wt% Fe to Cu/CeO₂ by wet-impregnation enhanced the activity for preferential oxidation of CO.¹⁹ The high CO oxidation activity of Fe–Cu oxides was reported by Cao et al.²⁰ They showed that mesoporous Fe–Cu composite oxide catalysts exhibited higher activity for and greater stability during low temperature CO oxidation compared with Fe and Cu oxide catalysts. Hornes et al. also reported the structural characterisation of 40 wt% Fe–Cu/CeO₂ for CH₄ oxidation.²¹ To the best of our knowledge, however, there are no published works related to the preparation of Fe–Cu/CeO₂ catalysts using a pulsed AP process.

In the present work, we have applied the dual-mode AP process to prepare Fe–Cu/CeO₂ catalysts. The structure of the catalysts was characterised by high-resolution transmission electron microscopy (HRTEM), X-ray photoelectron spectroscopy (XPS) and chemisorption measurements, and the structure was correlated with their catalytic activity for CO oxidation in comparison to Fe/CeO₂ and Cu/CeO₂. Our interest was also extended to compare the structures and catalytic properties of Fe–Cu/CeO₂ catalysts prepared by AP and wet-impregnation processes.

2. Material and methods

2.1 Catalyst preparation

Fe–Cu nanoparticles were prepared by pulsed cathodic AP using a procedure similar to that reported previously.^{5–10} The apparatus for the present purpose was equipped with two cathodic arc sources (Ulvac Inc., ARL-300): one with an Fe rod (99.9%, ϕ 10 mm, Furuya Metals Co., Ltd.) and the other with a Cu rod (99.9%, ϕ 10 mm, Furuya Metals Co., Ltd.) as

cathodes. Prior to the deposition of the Fe–Cu nanoparticles, a vacuum chamber was filled with N₂ and evacuated overnight to a pressure less than 1×10^{-3} Pa by a turbo-molecular pumping system to remove any gases adsorbed on CeO₂ (Rhodia Ltd.). A pulsed AP with a period of 0.2 ms and a current amplitude of 2 kA was generated with a frequency of 1 Hz. The nanoparticle size and deposition rate were controlled *via* the input energy, which is expressed by $E = (1/2) \cdot C \cdot V^2$, where C is the electric capacitance and V is the applied discharge voltage. The present study was performed using a capacitance and discharge voltage of 360 μF and 125 V, respectively. The generated plasmas entered into a container that contained CeO₂ powder (Brunauer–Emmett–Teller (BET) surface area: 173 m²·g⁻¹) under mechanical stirring. The metal loading was controlled by the number of pulses to be approximately 0.2 wt%. When the two pulses were triggered by a sole external input, the synchronous generation of two different plasmas was possible. Nanoparticles were also deposited on a TEM grid covered with a carbon film microgrid and/or γ-Al₂O₃ powders for the local structural analysis. Catalysts with the same composition were also prepared by a conventional wet-impregnation process using an aqueous solution of Fe(NO₃)₃ and/or Cu(NO₃)₂ and subsequent calcination at 600 °C for 3 h. The catalysts prepared by the AP and wet-impregnation processes are denoted as ‘AP’ and ‘imp’, respectively. As-prepared catalysts were thermally aged at 900 °C in a flow of 10% H₂O in air for 25 h to evaluate their thermal stability and catalytic activity.

2.2 Characterisation

X-ray diffraction (XRD) was performed using monochromated Cu-K_α radiation (30 kV, 30 mA, Rigaku Multiflex). The loading of Fe and/or Cu was determined using X-ray fluorescence (Rigaku EDXL300). HRTEM observations were performed using an FEI

TECNAI F20 electron microscope operated at 200 kV. The BET surface area (S_{BET}) was calculated from N_2 adsorption isotherms obtained at $-196\text{ }^\circ\text{C}$ (Belsorp-mini, BEL Japan, Inc.). Cu dispersion was determined without any reduction pretreatment using the pulsed CO technique (BELCAT-B, BEL Japan, Inc.). Before the CO pulses were applied, the catalyst was preheated in flowing He at $200\text{ }^\circ\text{C}$ for 30 min and subsequently cooled to a constant temperature of $50\text{ }^\circ\text{C}$. Cu dispersion was expressed in terms of CO/Cu, indicating the molar ratio of CO chemisorbed to Cu.

XPS was performed using monochromated Al- K_α radiation (12 keV, K-Alpha, Thermo) to measure Cu 2p and Ce 3d spectra, and Mg- K_α radiation (10 keV, ESCA-3400, Shimadzu) to measure Fe 2p spectra. The chemical shifts in the XPS spectra were corrected using the binding energy of C 1s at 285.0 eV. The intensity of the C 1s peak in the spectra of Fe, Cu and Fe-Cu/CeO₂ as-prepared using the AP process was approximately the same as that in the spectrum of neat CeO₂, suggesting that no measurable carbon deposition occurred during the AP preparation of the catalyst. The XPS analyses were performed without any pretreatment of the catalysts.

2.3 Catalytic reactions

Catalytic CO oxidation was performed in a flow reactor at atmospheric pressure. The as-prepared catalyst (10–20 mesh, 50 mg) was fixed in a quartz tube ($\phi 6\text{ mm}$) with quartz wool at both ends of the catalyst bed. The temperature dependence of the catalytic activity was evaluated by heating the catalyst bed from room temperature to $600\text{ }^\circ\text{C}$ at a constant rate of $10\text{ }^\circ\text{C}\cdot\text{min}^{-1}$ while supplying a gas mixture containing CO (0.1%), O₂ (1.25%) and He (balance) at $100\text{ cm}^3\cdot\text{min}^{-1}$ ($W/F = 5.0 \times 10^{-4}\text{ g}\cdot\text{min}\cdot\text{cm}^{-3}$). The concentration of CO and CO₂ in the effluent gas was analysed using a Horiba VA3000 NDIR on-line gas analyser.

In situ FT-IR spectroscopy was performed by a Nicolet 6700 spectrometer using a temperature-controllable diffuse-reflectance reaction cell with a KBr window connected to a gas supply system to enable measurements under controlled gas environments at atmospheric pressure. The sample was first preheated in situ in flowing He at 200 °C for 30 min prior to any experiment. Thereafter, the sample was cooled to 50 °C; the sample cell was subsequently purged with He and then filled with a gas mixture of 1% CO (He balance) for 10 min. Immediately after this procedure, the cell was flushed with a stream of He for 10 min at 50 °C; spectra were collected while the sample was under a stream of He and after the sample was supplied with 2.5% O₂/He for 10 min at the same temperature.

The dependence of the CO oxidation rate on the partial pressures of CO and O₂ was measured at 100 °C. Before the reaction, the catalysts were preheated in flowing He at 200 °C for 30 min and subsequently cooled to a constant temperature of 100 °C. The partial pressure of CO in the gas feed was varied from 0.05 to 0.1 kPa while the O₂ partial pressure was maintained at 1.25 kPa. The partial pressure of O₂ was then varied from 0.5 to 1.25 kPa while the CO partial pressure was maintained at 0.1 kPa.

CO oxidation using oxygen isotope was evaluated in pulse-mode reactions. The catalysts were preheated under flowing He at 300 °C for 30 min and were subsequently cooled to a constant temperature of 100–200 °C, where certain amounts of C¹⁶O (0.088 cm³) and ¹⁸O₂ (1.28 cm³) were simultaneously injected into the He stream. The product gas species in the effluent was monitored using a mass spectrometer (Omnistar, Pfeiffer) for the *m/e* values of 28(C¹⁶O), 30(C¹⁸O), 32(¹⁶O₂), 34(¹⁶O¹⁸O), 36(¹⁸O₂), 44(C¹⁶O₂), 46(C¹⁶O¹⁸O) and 48(C¹⁸O₂).

3. Results and Discussion

3.1 Local structure of Fe–Cu nanoparticles deposited by the AP process

The XRD patterns of the as-prepared Fe/CeO₂, Cu/CeO₂ and Fe–Cu/CeO₂ using AP and wet-impregnation processes exhibited peaks assignable to CeO₂ with a cubic fluorite-type structure (Figure S1 in ESI† for XRD patterns). After the samples were thermally aged at 900 °C, the diffraction peaks of CeO₂ became intense and sharp because of sintering, whereas other diffraction peaks associated with Fe, Cu and Fe–Cu were not observed because of their low loading levels of 0.1–0.2 wt%. The TEM observation was carried out using Fe, Fe–Cu and Cu nanoparticles as deposited on TEM grids covered with a carbon-film microgrid. Figure 1a–c shows these TEM images together with size distributions of nanoparticles. All these histogram analyses are similar, indicating very narrow size distributions ranging from 1 to 5 nm with an average size of 2.7–2.9 nm. As is evident from our previous studies, Rh, Pd, Pt and/or Fe–Pd nanoparticles with almost the same size distributions could be obtained by AP under the same condition.^{6–8, 10} Figure 1d shows a TEM image of Fe–Cu/CeO₂ as prepared by AP. Because Fe–Cu nanoparticle with the size of 2–3 nm could be observed on CeO₂ nanoparticles (shown by a white arrow), the size of the Fe–Cu nanoparticles deposited on CeO₂ are similar to that of the unsupported Fe–Cu nanoparticles shown in Figure 1c. TEM observation was also carried out for Fe–Cu/CeO₂ after thermal aging at 900 °C, which caused a significant grain growth of CeO₂ to several hundred nanometers. However, it was impossible to discriminate Fe–Cu particles from the background of grown CeO₂ particles having a high contrast. The structure of nanoparticles in the Fe–Cu system prepared by AP was further analysed by the local structural analysis using focused beams and EDX technique. Figure 1e demonstrates EDX spectrum taken from a region containing one unsupported Fe–Cu nanoparticle shown in Figure 1f, which was prepared by AP. Because as-deposited

single nanoparticle contained both Fe and Cu (Fe: 58 wt%, Cu: 42 wt%), it is considered that dual arc-plasma generation should be useful for the deposition of binary nanoparticles.

According to our previous study on a Pd–Fe bimetal system prepared by the pulsed arc-plasma technique,¹⁰ synchronizing two plasma sources (Pd and Fe) triggered by the single external input is a key to yield the bimetal nanoparticles. Under such a synchronous condition, two plasmas as generated from two sources reach to the substrate surface nearly simultaneously. Two metal species then diffuse on the surface with losing their kinetic energy, and finally collide with each other to deposit bimetal (composite) nanoparticles. When the two pulses are not synchronized, the situation is totally different; one metal species will not collide with the other metal species because the period of pulsed plasma is very short (<200 μ s) and two metal species are therefore deposited separately.

The oxidation state of Fe–Cu nanoparticles deposited on CeO₂ was characterized by XPS using the samples prepared by wet-impregnation as references. The intensity of each spectrum was normalised by the Ce 3d. As shown in Figure 2, the Fe 2p XPS spectra of as-prepared Fe/CeO₂(AP) and Fe–Cu/CeO₂(AP) exhibited two Fe 2p_{3/2} peaks assignable to Fe⁰ and Fe³⁺ at 707.0 and 711.5 eV, respectively. Additionally, the shake-up satellite peak associated with the presence of Fe³⁺ was observed at the higher binding energy side than its Fe 2p_{3/2} peak. Although the AP process under vacuum yielded metallic nanoparticles, they should be oxidised when exposed to atmospheric air. As-prepared Fe–Cu/CeO₂(AP) (Fe⁰: 24%, Fe³⁺: 76%) contained more Fe³⁺ than Fe/CeO₂(AP) (Fe⁰: 43%, Fe³⁺: 57%). It should be noted that these two species in Fe/CeO₂(AP) disappeared after the thermal aging to give rise to a sole peak assignable to Fe²⁺ at 709.0 eV. This is complete contrast to Fe–Cu/CeO₂(AP), the abundance of Fe³⁺ remained almost unchanged (Fe²⁺: 30%, Fe³⁺: 70%). This is not the case of the sample prepared by wet-impregnation; Fe/CeO₂(imp) and Fe–Cu/CeO₂(imp)

showed a peak due to Fe^{2+} before and after thermal aging. For all these catalysts, the surface concentrations of Fe, $(\text{Fe}/\text{Ce})_s$, did not change during the thermal aging. In addition, no noticeable difference of $(\text{Fe}/\text{Ce})_s$ was found between $\text{Fe}-\text{Cu}/\text{CeO}_2(\text{AP})$ and $\text{Fe}-\text{Cu}/\text{CeO}_2(\text{imp})$ (Table 1).

Figure 3 shows the Cu 2p XPS spectra for Cu/CeO_2 and $\text{Fe}-\text{Cu}/\text{CeO}_2$, which were prepared by AP and wet-impregnation. The deconvolution of the observed peaks revealed two sets of spin-orbital doublets assigned to Cu^+ and Cu^{2+} . The two satellite peaks (940.0 and 944.0 eV) attributed to Cu^{2+} with $3d^9$ electronic state were also found. Unlike the Fe 2p spectra in Figure 2, the as-prepared $\text{Cu}/\text{CeO}_2(\text{AP})$ and $\text{Fe}-\text{Cu}/\text{CeO}_2(\text{AP})$ showed very weak Cu 2p peaks, although they were intensified significantly after the samples were thermally aged at 900 °C. This is indicative of the positive effect of thermal aging on surface concentrations of Cu on CeO_2 . As was evident from very weak shake-up satellite assignable to Cu^{2+} , a large part of Cu should be monovalent (Cu^+). The fraction of Cu^+ (Cu^+/Cu) on the surface was calculated as shown in Table 1. Both samples after aging contained high fractions of Cu^+ (~80%) and the similar trend was also observed for the samples prepared by wet-impregnation. The surface concentrations of Cu, $(\text{Cu}/\text{Ce})_s$, were in the range of 0.04–0.06, which were less than those of Fe. The catalysts prepared by AP showed higher $(\text{Cu}/\text{Ce})_s$ compared to the impregnated catalysts. The Ce 3d XPS spectra of these samples were also measured (Figure S2 in ESI† for XPS spectra), but no noticeable difference was observed. The Ce^{3+}/Ce surface concentration ratio was in the range of 17–25%, which was the same as that for the neat CeO_2 (Table S1 for in ESI† for physicochemical properties). Summarising these XPS results, it is concluded that thermally aged $\text{Fe}-\text{Cu}/\text{CeO}_2(\text{AP})$ contained Fe^{3+} and Cu^+ , whereas Fe^{2+} and Cu^{2+} were more abundant in the impregnated sample.

3.2 Catalytic activity of Fe–Cu/CeO₂(AP) for CO oxidation

Figure 4 compares light-off curves for CO oxidation over Fe/CeO₂(AP), Cu/CeO₂(AP), Fe–Cu/CeO₂(AP) and Fe–Cu/CeO₂(imp) before and after the samples were thermally aged at 900 °C. The activity of as-prepared catalysts exhibited the following sequence of increasing value: Fe/CeO₂(AP) < Fe–Cu/CeO₂(AP) < Cu/CeO₂(AP) < Fe–Cu/CeO₂(imp). However, thermally aged samples showed completely different catalytic behaviours. Although Fe/CeO₂(AP) was significantly deactivated, other samples containing Cu showed enhanced activities, despite the significant loss of surface area from 170 m²·g⁻¹ to less than 10 m²·g⁻¹ due to the sintering of CeO₂. The extent of the activity enhancement was most obvious for Fe–Cu/CeO₂(AP), which showed the highest activity after thermal aging. The stability of aged Fe–Cu/CeO₂(AP) was tested at 150 °C, but no indication of noticeable deactivation was observed during 2 h of reaction (Figure S3 in ESI† for CO oxidation activity test).

To elucidate the reason for the high catalytic activity of thermally aged Fe–Cu/CeO₂(AP), in situ FT-IR spectra of adsorbed CO were measured at 50 °C without any reduction pretreatment (Figure 5). Under flowing 1% CO/He, Cu/CeO₂(AP) and Fe–Cu/CeO₂(AP) showed a peak assignable to the CO stretching vibration mode in contrast to negligible peaks on Fe/CeO₂(AP). The aged Cu/CeO₂(AP) exhibited an adsorption band at 2098 cm⁻¹ assignable to linear CO species adsorbed on Cu. Fe–Cu/CeO₂(AP) also showed more intense band at 2107 cm⁻¹. This is indicative of the larger molar ratio of CO adsorbed and Cu loaded (CO/Cu) in consistent with higher surface concentration of Cu, (Cu/Ce)_s, as shown in Table 1. Although the band became less intense after the gas feed was changed to He, Fe–Cu/CeO₂(AP) still preserved the higher intensity than Cu/CeO₂(AP). When O₂ was subsequently supplied, the adsorbed CO species were soon consumed by catalytic oxidation

(Figure 5c). This was supported by the evolution of CO₂, which was detected by parallel on-line mass spectroscopy. In situ FT-IR spectra of CO adsorbed on the as-prepared catalysts were also measured (Figure S4 in ESI† for FT-IR spectra). The as-prepared Fe, Cu and Fe–Cu/CeO₂(AP) catalysts showed only very weak CO bands in a flow of 1% CO and He. Moreover, these bands soon disappeared after the gas feed was changed to He. Because these behaviours were completely different from those of thermally aged catalysts shown in Figure 5, the surface Cu⁺ site, which formed on the surface of CeO₂ by thermally aging at 900 °C, is responsible for the CO adsorption.

The catalytic properties of thermally aged catalysts are summarized in Table 1. Cu/CeO₂(AP) exhibited larger Cu⁺/Cu and CO/Cu values compared with Cu/CeO₂(imp). This effect of the preparation method was more pronounced for Fe–Cu/CeO₂, where AP achieved a CO/Cu value (0.62) approximately five-fold larger than the impregnated sample (0.11). It should also be noted that Fe–Cu/CeO₂(AP) showed a larger CO/Cu value compared to Cu/CeO₂(AP). This implies that Fe plays a key role in promoting Cu dispersion on the CeO₂ surface. Because of these advantageous features, aged Fe–Cu/CeO₂(AP) exhibited the lowest light-off temperature (T₅₀), which is defined as temperature at which CO conversion reached 50%. The turnover frequency (TOF) was calculated using the CO conversion rate at 100 °C and apparent Cu loading (Table 1). Fe–Cu/CeO₂(AP) showed the highest TOF among the studied samples, whereas Cu/CeO₂(imp) and Cu/CeO₂(AP) showed the TOF values comparable to literature data of Cu–CeO₂ catalysts.¹⁴ On the basis of these results, we concluded that the higher CO oxidation activity of thermally aged Fe–Cu/CeO₂(AP) is associated with the highly dispersed active Cu⁺ site, which was successfully formed on the CeO₂ surface after thermal aging.

As shown in Figures 3, 4, and 5, the activity enhancement by thermal aging also occurred in Cu/CeO₂(AP) in accordance with increased CO adsorption onto Cu⁺ on the CeO₂ surface. This is of interest with regard to the interaction between Cu and CeO₂, although the mechanism is still unclear at this moment. According to previous studies on Cu–CeO₂ system,^{25–32} a variety of Cu species are known to form depending on the preparation method and condition; a bulk Cu oxide, isolated Cu ions incorporated in the CeO₂ lattice, and/or surface Cu ions. Several theoretical calculation studies have been performed to elucidate the Cu–CeO₂ interactions. Yang et al. reported density-functional theory (DFT) calculations on the structure of Cu-doped CeO₂(111) surface and found that Cu is stable both as an adsorbed atom (Cu⁺) on the surface and as a dopant (Cu²⁺) in the surface region.²⁵ Wong et al. also applied DFT calculations to the CeO₂(111) surface modified with Cu and suggested that tunneling of Cu–O antibonding electrons into empty Ce 4f states via the Cu–O–Ce bonding at the interface stabilizes the Cu layer on the surface of CeO₂.²⁶ With these information taken into consideration, the interfacial bonding is considered to play a primary role of high Cu dispersion after thermal ageing. Because the present Fe–Cu/CeO₂(AP) catalyst showed a larger CO/Cu value compared to Cu/CeO₂(AP) (Table 1), it should also be noted that Fe further promotes the Cu dispersion on the CeO₂ surface. One possibility is that the formation of Fe³⁺–Cu⁺ oxide moiety bound to the CeO₂ surface enhances the formation and the dispersion of Cu⁺ species. The Fe³⁺–Cu⁺ oxide moiety may be difficult to form in catalysts prepared by wet-impregnation, probably because of the very low metal loading (0.2 wt%). By contrast, the AP process deposits Fe–Cu bimetal nanoparticles and thus enables more efficient formation of Fe³⁺–Cu⁺ oxide moiety on the CeO₂ surface. Further structural characterization using X-ray absorption fine structure (XAFS) is now under investigation.

3.3 Possible reaction mechanism of CO oxidation

To study the reaction mechanism of CO oxidation over thermally aged Cu/CeO₂(AP) and Fe–Cu/CeO₂(AP), we measured the dependence of the CO oxidation rate on the partial pressures of CO and O₂ at 100 °C (Figure 6). Both Cu/CeO₂(AP) and Fe–Cu/CeO₂(AP) showed linear relationships between the logarithmic reaction rates and the partial pressures of CO and O₂, indicating partial orders of ~0.9 and ~0.0 with respect to CO and O₂, respectively. These partial orders suggested that the adsorption of CO on Cu (Cu⁺) is slow, whereas the adsorption of gaseous O₂ on the catalyst surface is rapid. This implies that the lattice oxygen on the surface play a role as a reactant for adsorbed CO. To demonstrate this hypothesis, pulse reactions between C¹⁶O and ¹⁸O₂ were performed to elucidate the role of lattice oxygen. Figure 7 shows the fraction of C¹⁶O₂ in the CO₂ product for a pulsed C¹⁶O–¹⁸O₂ reaction at different temperatures over Cu/CeO₂(AP) and/or Fe–Cu/CeO₂(AP) after the catalysts were thermally aged. At 100 °C, the pulsing to Cu/CeO₂(AP) generated C¹⁶O₂ more than 80% of total CO₂. Fe–Cu/CeO₂(AP) yielded a little smaller C¹⁶O₂ fractions, although they were still larger than 70%. These results demonstrated that the absorbed CO mostly reacts with the lattice oxygen on the surface. This is consistent with the partial reaction orders (Figure 6) and is indicative of the CO oxidation *via* the Mars–van Krevelen mechanism. The fractions of C¹⁶O₂ tended to decrease with increasing reaction temperature, indicating that increasing fractions of the adsorbed CO reacts with the dissociatively adsorbed oxygen at elevated temperatures.

4. Conclusions

The dual-mode AP technique could successfully deposit Fe–Cu bimetal nanoparticles onto CeO₂ powders. Thermal aging of as-prepared sample with very small metal loading (~0.2

wt%) enables the formation of Fe–Cu oxide on the CeO₂ surface, which is an efficient catalyst for CO oxidation. During thermal aging at 900 °C, a monovalent copper (Cu⁺) was formed as the active site for CO oxidation. Fe plays a role of a promoter to enable the higher Cu dispersion in spite of significant sintering of CeO₂. Because such highly dispersed Cu⁺ species were less abundant when Fe–Cu/CeO₂ was prepared by conventional wet-impregnation technique, or when Cu was solely deposited by AP on CeO₂. The rate of CO oxidation over the thermally aged Fe–Cu/CeO₂(AP) was independent of the partial pressure of O₂ and the CO adsorbed on Cu⁺ reacts primarily with the lattice oxygen. These results indicate that CO oxidation is considered to proceed *via* the Mars–van Krevelen mechanism.

Acknowledgements

This study was supported by the MEXT program ‘Elements Strategy Initiative to Form Core Research Centers’.

References

1. M. Boutonnet Kizling and S. G. Järås, *Appl. Catal. A: General*, 1996, **147**, 1–21.
2. Z. R. Ismagilov, O. Y. Podyacheva, O. P. Solonenko, V. V. Pushkarev, V. I. Kuz'min, V. A. Ushakov and N. A. Rudina, *Catal. Today*, 1999, **51**, 411–417.
3. C.-j. Liu, G. P. Vissokov and B. W. L. Jang, *Catal. Today*, 2002, **72**, 173–184.
4. H. Shim, J. Phillips, I. M. Fonseca and S. Carabinerio, *Appl. Catal. A: General*, 2002, **237**, 41–51.
5. S. Hinokuma, K. Murakami, K. Uemura, M. Matsuda, K. Ikeue, N. Tsukahara and M. Machida, *Topics Catal.*, 2009, **52**, 2108–2111.
6. S. Hinokuma, M. Okamoto, E. Ando, K. Ikeue and M. Machida, *Catal. Today*, 2011, **175**, 593–597.
7. S. Hinokuma, M. Okamoto, E. Ando, K. Ikeue and M. Machida, *Bull. Chem. Soc. Jpn.*, 2012, **85**, 144–149.
8. S. Hinokuma, H. Fujii, Y. Katsuhara, K. Ikeue and M. Machida, *Catal. Sci. Technol.*, 2014, **4**, 2990–2996.
9. S. Hinokuma, H. Kogami, N. Yamashita, Y. Katsuhara, K. Ikeue and M. Machida, *Catal. Commun.*, 2014, **54**, 81–85.
10. S. Hinokuma, Y. Katsuhara, E. Ando, K. Ikeue and M. Machida, *Catal. Today*, 2013, **201**, 92–97.

11. W. Liu and M. Flytzani-Stephanopoulos, *J. Catal.*, 1995, **153**, 304–316.
12. R. Sundar and S. Deevi, *J. Nanoparticle Res.*, 2006, **8**, 497–509.
13. C. Shiau, M. Ma and C. Chuang, *Appl. Catal. A-General*, 2006, **301**, 89–95.
14. M. Luo, J. Ma, J. Lu, Y. Song and Y. Wang, *J. Catal.*, 2007, **246**, 52–59.
15. M. Yakimova, V. Ivanov, O. Polezhaeva, A. Trushin, A. Lermontov and Y. Tretyakov, *Dokl. Chem.*, 2009, **427**, 186–189.
16. H. Wan, D. Li, Y. Dai, Y. Hu, Y. Zhang, L. Liu, B. Zhao, B. Liu, K. Sun, L. Dong and Y. Chen, *Appl. Catal. A-General*, 2009, **360**, 26–32.
17. D. Zhang, Y. Qian, L. Shi, H. Mai, R. Gao, J. Zhang, W. Yu and W. Cao, *Catal. Commun.*, 2012, **26**, 164–168.
18. L. Qi, Q. Yu, Y. Dai, C. Tang, L. Liv, H. Zhang, F. Gao, L. Dong and Y. Chen, *Appl. Catal. B-Environmental*, 2012, **119**, 308–320.
19. Z. Lenzion-Bielun, M. Bettahar and S. Monteverdi, *Catal. Commun.*, 2010, **11**, 1137–1142.
20. J. Cao, Y. Wang, X. Yu, S. Wang, S. Wu and Z. Yuan, *Appl. Catal. B-Environmental*, 2008, **79**, 26–34.
21. A. Hornes, G. Munuera, A. Fuerte, M. Escudero, L. Daza and A. Martinez-Arias, *J. Power Sources*, 2011, **196**, 4218–4225.

22. K. Sirichalprasert, A. Luengnaruemitchai and S. Pongstabodee, *Int. J. Hydrogen Energy*, 2007, **32**, 915–926.
23. J. Li, Y. Han, Y. Zhu and R. Zhou, *Appl. Catal. B-Environmental*, 2011, **108**, 72–80.
24. G. Kaur and S. Basu, *J. Power Sources*, 2013, **241**, 783–790.
25. Z. Yang, B. He, Z. Lu and K. Hermansson, *J. Phys. Chem. C*, 2010, **114**, 4486–4494.
26. K. Wong, Q. Zeng and A. Yu, *Chem. Eng. J.*, 2011, **174**, 408–412.
27. M. Fernandez-Garcia, E. Rebollo, A. Ruiz, J. Conesa and J. Soria, *J. Catalysis*, 1997, **172**, 146–159.
28. S. Hocevar, U. Krasovec, B. Orel, A. Arico and H. Kim, *Appl. Catal. B-Environmental*, 2000, **28**, 113–125.
29. G. Avgouropoulos, T. Ioannides and H. Matralis, *Appl. Catal. B-Environmental*, 2005, **56**, 87–93.
30. P. Djinovic, J. Batista and A. Pintar, *Appl. Catal. A-General*, 2008, **347**, 23–33.
31. R. Kydd, W. Teoh, K. Wong, Y. Wang, J. Scott, Q. Zeng, A. Yu, J. Zou and R. Amal, *Adv. Funct. Mater.*, 2009, **19**, 369–377.
32. M. Branda, N. Hernandez, J. Sanz and F. Illas, *J. Phys. Chem. C*, 2010, **114**, 1934–1941.

Table 1 Compositions and catalytic properties of Fe, Cu and Fe–Cu/CeO₂ catalysts after thermally aged at 900 °C for 25 h in 10% H₂O/air

Fe	Cu		Cu ⁺ /Cu ^a	(Fe/Ce) _s ^b	(Cu/Ce) _s ^b	CO _{ads} ^c	CO/Cu ^d	T ₅₀ ^e	TOF ^f
/ wt%	/ wt%					/ μmol·g ⁻¹		/ °C	/ 10 ⁻² s ⁻¹
0.18	0.11	AP	0.79	0.12	0.061	10.7	0.62	158	1.9
0.17	0.11	imp	0.66	0.13	0.042	1.9	0.11	235	1.3
-	0.15	AP	0.89	-	0.051	5.7	0.24	170	1.2
-	0.13	imp	0.84	-	0.038	3.7	0.18	263	1.1
0.20	-	AP	-	0.11	-	0.3	-	447	-

^a Fraction of Cu⁺ determined from Cu 2p XPS spectra.

^b Surface concentration determined from Fe 2p, Cu 2p and Ce 3d XPS spectra.

^c Amount of chemisorbed CO.

^d Molar ratio of chemisorbed CO and loaded Cu.

^e Temperature at which CO conversion reached 50%.

^f Turnover frequency calculated by using the CO conversion rate at 100 °C and apparent Cu loading.

Figure captions

Figure 1 TEM images, size distributions and average sizes of unsupported (a) Fe, (b) Cu (c) Fe–Cu nanoparticles and (d) Fe–Cu/CeO₂ prepared by the AP process; (e) An EDX spectrum taken from (f) a region containing one unsupported Fe–Cu nanoparticle shown by a white circle.

Figure 2 Fe 2p XPS spectra of (left) Fe/CeO₂ and (right) Fe–Cu/CeO₂ prepared by (a, b) the AP and (c, d) wet-impregnation processes; spectra were collected (a, c) before and (b, d) after the catalysts were thermally aged at 900 °C for 25 h.

Figure 3 Cu 2p XPS spectra of (left) Cu/CeO₂ and (right) Fe–Cu/CeO₂ prepared by (a, b) the AP and (c, d) wet-impregnation processes; spectra were collected (a, c) before and (b, d) after the catalysts were thermally aged at 900 °C for 25 h.

Figure 4 Temperature dependence of CO oxidation over Fe/CeO₂(AP), Cu/CeO₂(AP), Fe–Cu/CeO₂(AP) and Fe–Cu/CeO₂(imp) before and after the catalysts were thermally aged at 900 °C for 25 h. Reaction conditions: 0.1% CO, 1.25% O₂, He balance, W/F = 5.0×10^{-4} g·min·cm⁻³.

Figure 5 In situ FT-IR spectra of CO adsorbed on Fe, Cu and Fe–Cu/CeO₂(AP) at 50 °C after the catalysts were aged at 900 °C for 25 h. The spectra were measured in gas feeds of (a) 1% CO and He balance, followed by (b) He and (c) 2.5% O₂ and He balance.

Figure 6 Dependence of the CO oxidation rate on the partial pressures of CO and O₂ at 100 °C

over Cu/CeO₂(AP) and Fe–Cu/CeO₂(AP) after thermal aging at 900 °C for 25 h. Numbers in figures show partial orders.

Figure 7 Fraction of C¹⁶O₂ in the CO₂ product for the C¹⁶O–¹⁸O₂ reaction at different temperatures over Cu/CeO₂(AP) and Fe–Cu/CeO₂(AP) after the catalysts were thermally aged at 900 °C for 25 h.

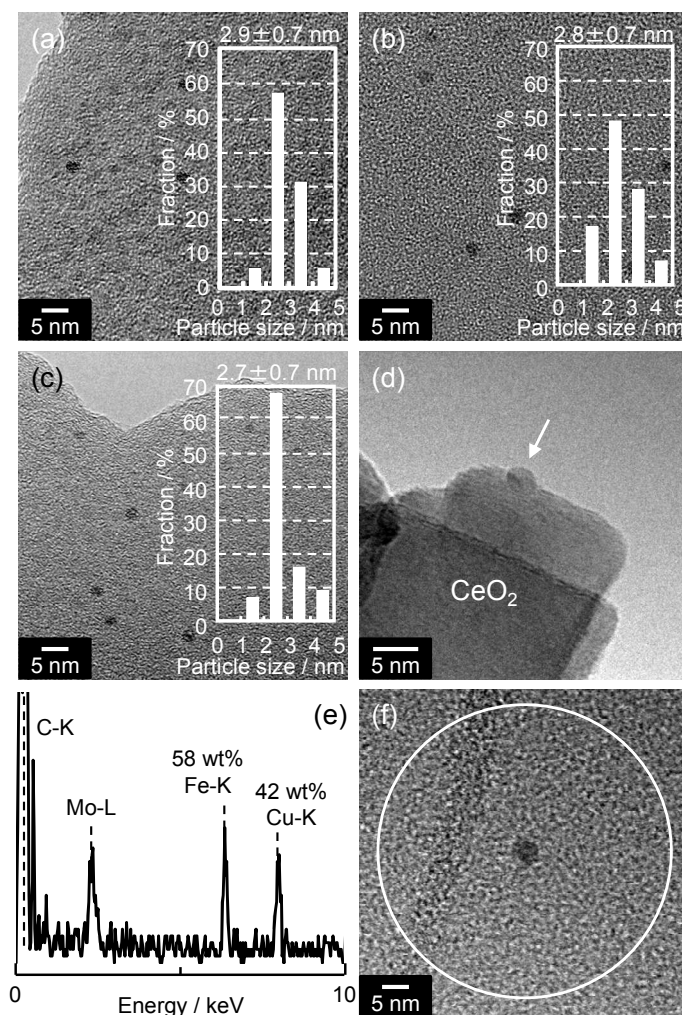


Figure 1 TEM images, size distributions and average sizes of unsupported (a) Fe, (b) Cu (c) Fe-Cu nanoparticles and (d) Fe-Cu/CeO₂ prepared by the AP process; (e) An EDX spectrum taken from (f) a region containing one unsupported Fe-Cu nanoparticle shown by a white circle.

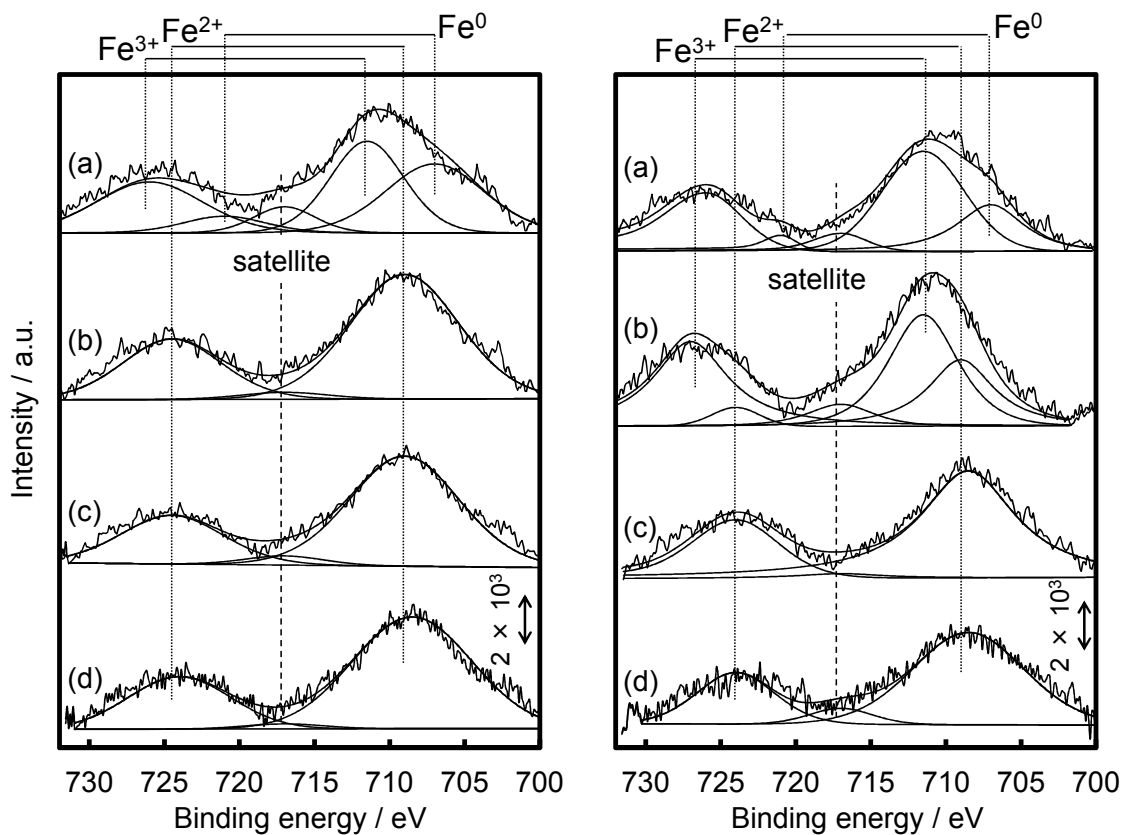


Figure 2 Fe 2p XPS spectra of (left) Fe/CeO₂ and (right) Fe–Cu/CeO₂ prepared by (a, b) the AP and (c, d) wet-impregnation processes; spectra were collected (a, c) before and (b, d) after the catalysts were thermally aged at 900 °C for 25 h.

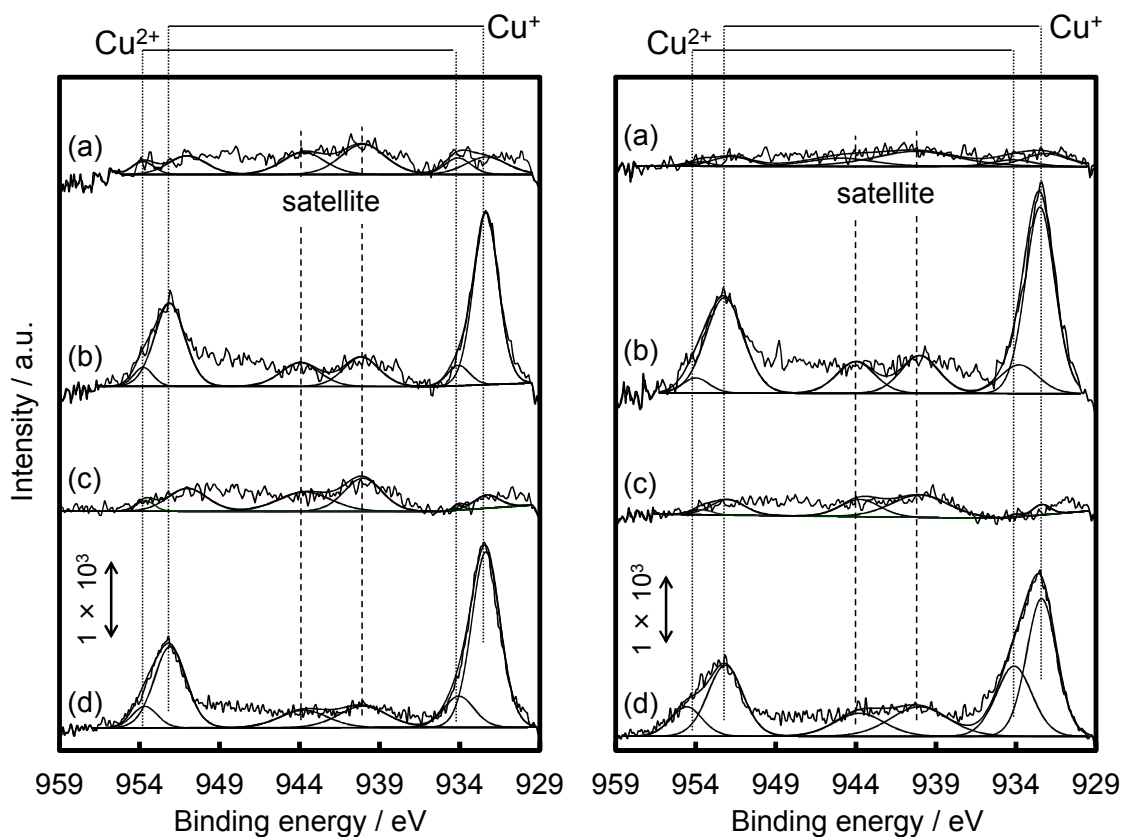


Figure 3 Cu 2p XPS spectra of (left) Cu/CeO₂ and (right) Fe–Cu/CeO₂ prepared by (a, b) the AP and (c, d) wet-impregnation processes; spectra were collected (a, c) before and (b, d) after the catalysts were thermally aged at 900 °C for 25 h.

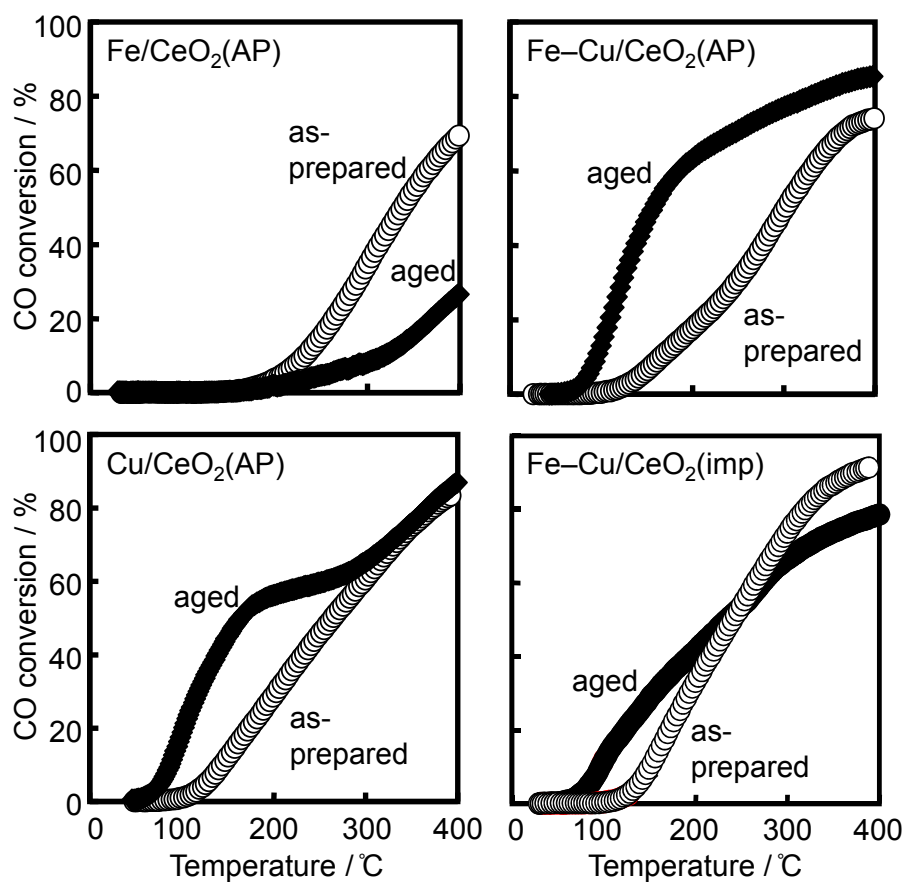


Figure 4 Temperature dependence of CO oxidation over Fe/CeO₂(AP), Cu/CeO₂(AP), Fe-Cu/CeO₂(AP) and Fe-Cu/CeO₂(imp) before and after the catalysts were thermally aged at 900 °C for 25 h. Reaction conditions: 0.1% CO, 1.25% O₂, He balance, W/F = 5.0×10^{-4} g·min·cm⁻³.

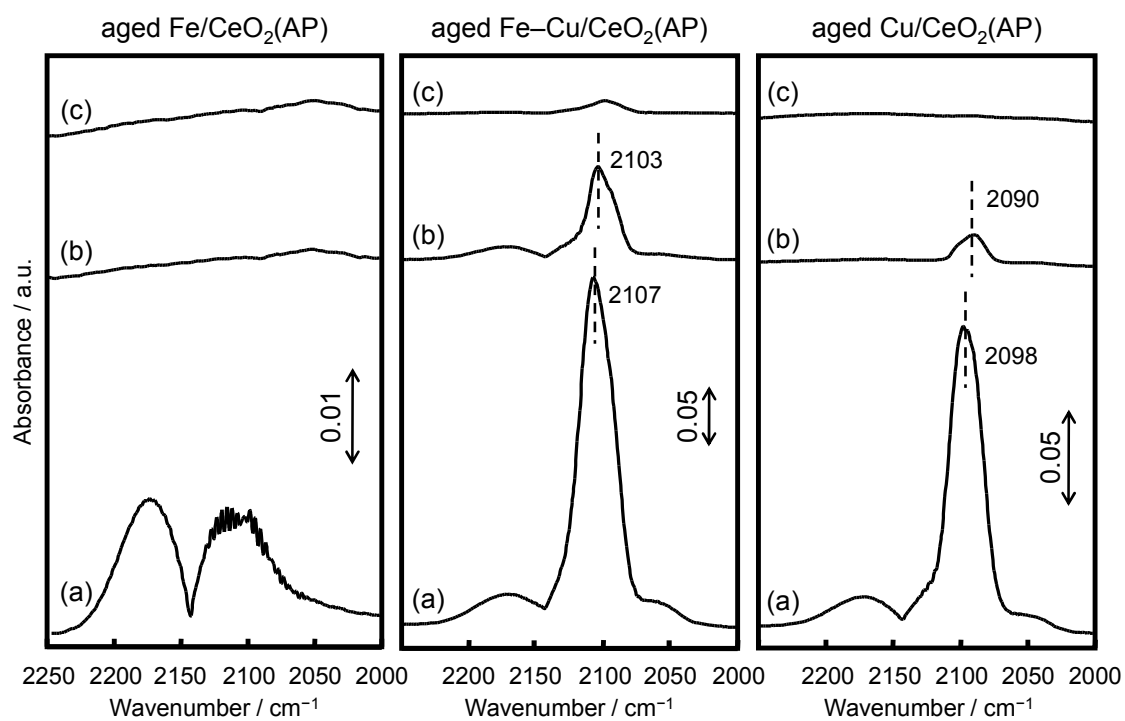


Figure 5 In situ FT-IR spectra of CO adsorbed on Fe, Cu and Fe–Cu/CeO₂(AP) at 50 °C after the catalysts were aged at 900 °C for 25 h. The spectra were measured in gas feeds of (a) 1% CO and He balance, followed by (b) He and (c) 2.5% O₂ and He balance.

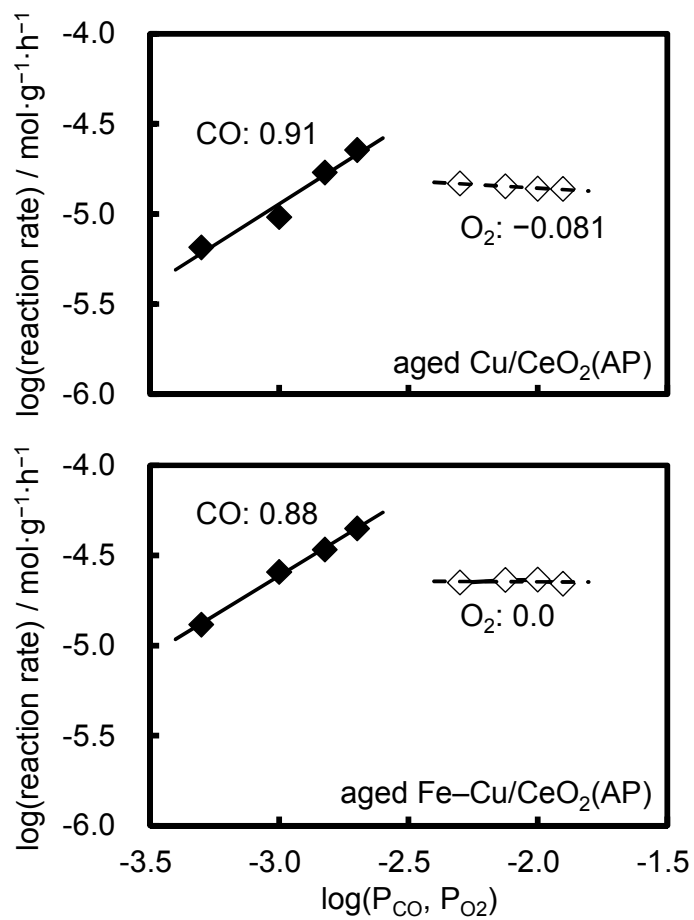


Figure 6 Dependence of the CO oxidation rate on the partial pressures of CO and O₂ at 100 °C over Cu/CeO₂(AP) and Fe-Cu/CeO₂(AP) after thermal aging at 900 °C for 25 h. Numbers in figures show partial orders.

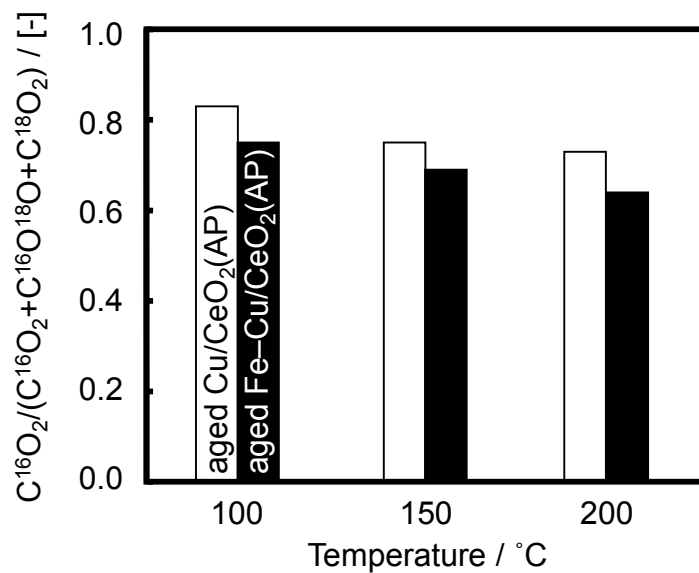
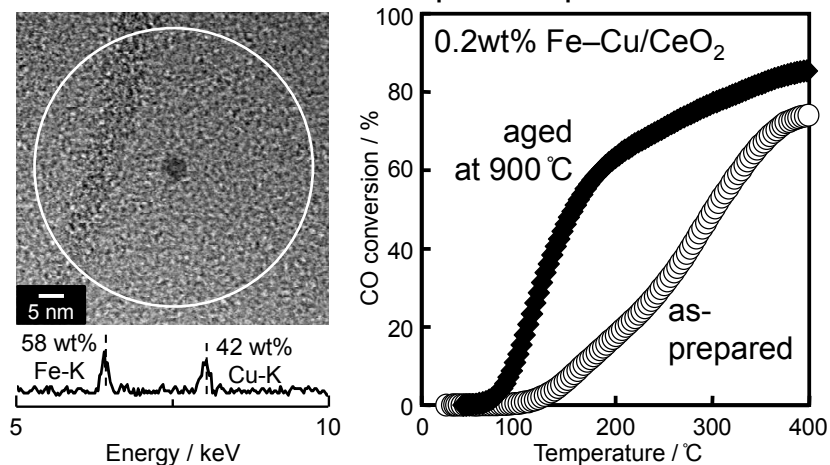


Figure 7 Fraction of C¹⁶O₂ in the CO₂ product for the C¹⁶O–¹⁸O₂ reaction at different temperatures over Cu/CeO₂(AP) and Fe–Cu/CeO₂(AP) after the catalysts were thermally aged at 900 °C for 25 h.

Graphical abstract

Fe–Cu bimetal nanoparticles deposited by the dual-mode arc-plasma process



Highlights

Fe–Cu bimetal nanoparticles were prepared by the dual-mode arc-plasma process. The CO oxidation activity of Fe–Cu/CeO₂ was enhanced by thermal ageing at 900 °C. CO oxidation over aged Fe–Cu/CeO₂ proceeded *via* the Mars–van Krevelen mechanism.